T. Dang, Z. Liu, X.W. Zhou, Y. Sun, P.G. Zhao
Dynamic Response of a Hypersonic Rocket Sled Considering Friction and Wear
Journal of Spacecraft and Rockets, Vol. 59, N. 4, 2022, p. 1289-1303
doi:10.2514/1.A35267

Dynamic Response of a Hypersonic Rocket Sled considering Friction and Wear

Tianjiao Dang,[1] and Zhen Liu.[2]
State Key Laboratory for Strength and Vibration of Mechanical Structures, Shaanxi Key Laboratory of Environment and Control for Flight Vehicle, School of Aerospace Engineering, Xi'an Jiaotong University, Xi'an, Shaanxi, 710049, P.R. China

Xuewen Zhou,[3]
Norinco Group Test and Measuring Academy, Huayin, Shaanxi, 714200, P.R. China

Ye Sun,[4] and Penggang Zhao.[5]
State Key Laboratory for Strength and Vibration of Mechanical Structures, Shaanxi Key Laboratory of Environment and Control for Flight Vehicle, School of Aerospace Engineering, Xi'an Jiaotong University, Xi'an, Shaanxi, 710049, P.R. China

The dynamic response of a hypersonic rocket sled was studied by considering the time-varying friction coefficient and the gap caused by wear between the slipper and track. A multi-body dynamic model for a hypersonic rocket sled system was established by considering the time-varying mass and moment of inertia, nonlinear aerodynamic loads, engine thrust, track irregularity, and nonlinear contact force. As for the wear calculation, the ductile and shear criteria were used as the material damage criteria, and slipper wear was determined by the number of damaged elements. A rocket sled test was also carried out, and the dynamic response of the sled was measured. The results showed that the computational sliding displacement and velocity of the third-stage sled matched well with the test values. The computational root mean square (RMS) values of the vertical acceleration of the third-stage sled front slipper considering friction and wear matched better with the test values than with the case without considering friction and wear, which underestimated the RMS value by approximately 20.1% at Mach 5. The importance of considering friction and wear and the correctness of the computational method were

[1] PhD Student, School of Aerospace Engineering.
[2] Associate Professor and Corresponding Author, School of Aerospace Engineering, Email: liuz@mail.xjtu.edu.cn.
[3] Senior Scientist, Rocket Sled Test Center.
[4] PhD Student, School of Aerospace Engineering.
[5] Graduate Student, School of Aerospace Engineering.

validated. It is also found that the kinetic friction coefficient decreased with an increase in the product of the pressure and velocity. The wear height of the slipper increased almost linearly with the sliding displacement. The test results showed that the vertical acceleration power spectral density of the third-stage sled front slipper increased with time in the full frequency band below 2000 Hz. This study will guide the design and optimisation of hypersonic rocket sleds.

Nomenclature

A	=	slipper–track contact area
$\boldsymbol{a}$	=	acceleration
b	=	directionally dependent material parameter in ductile fracture curve
c	=	damping constant
$\boldsymbol{D}$	=	aerodynamic drag
$DMAX$	=	maximum penetration depth
e	=	exponent in L-N contact force formula
$\boldsymbol{F}_n$	=	slipper–track normal contact force
$\boldsymbol{F}_t$	=	slipper–track tangential contact force (frictional force)
f	=	material parameter in shear fracture curve
$\boldsymbol{G}$	=	gravity
g	=	current penetration depth
H	=	length of the third-stage sled
h	=	wear height
J	=	moment of inertia
K	=	contact stiffness
k_S	=	material parameter in shear fracture curve
$\boldsymbol{L}$	=	aerodynamic lift
l	=	step size of backward differentiation formula
$\mathbf{M}$	=	mass matrix

55	m	=	mass
56	Ma	=	Mach number
57	$\boldsymbol{M}_p$	=	aerodynamic pitch moment
58	$\boldsymbol{n}$	=	normal unit vector
59	$\mathbf{n}_{\perp}$	=	tangential unit vector
60	P	=	normal pressure
61	PV value	=	product of normal pressure and sliding velocity
62	$\mathbf{q}$	=	generalised coordinates
63	$\boldsymbol{s}$	=	displacement
64	$\boldsymbol{T}$	=	engine thrust
65	t	=	time
66	$\triangle t$	=	time step
67	t_1	=	moment when the first-stage sled separates
68	t_2	=	moment when the second-stage sled separates
69	t_{total}	=	total time
70	$\boldsymbol{v}$	=	velocity
71	w	=	wear rate
72	$\boldsymbol{\beta}$	=	attitude angle
73	γ	=	second order derivative term in dynamic equations
74	ε_D	=	ductile strain
75	ε_D^{**}	=	equivalent fracture strain at ductile fracture
76	ε_S	=	shear strain
77	ε_S^{**}	=	equivalent fracture strain at shear fracture
78	$\varepsilon_S^+ / \varepsilon_S^-$	=	equivalent plastic strain in equibiaxial tension/compression at shear fracture
79	$\varepsilon_T^+ / \varepsilon_T^-$	=	equivalent plastic strain in equibiaxial tension/compression at ductile fracture
80	η	=	stress triaxiality

η^+ / η^-	=	stress triaxiality in equibiaxial tension/compression at ductile fracture
θ	=	shear stress parameter
θ^+ / θ^-	=	shear stress parameter for equibiaxial tension/compression
λ	=	Lagrange multiplier
μ	=	kinetic friction coefficient
ϕ	=	ratio of maximum shear stress to equivalent stress
φ	=	coefficient of backward differentiation formula
$\mathbf{\Phi}_q$	=	Jacobian matrix
ψ	=	coefficient of backward differentiation formula

Subscripts

x, *y*, *z*	=	sliding direction, vertical direction, lateral direction

I. Introduction

A hypersonic rocket sled is a large, high-precision ground-test equipment mainly used to solve a series of test problems associated with aerodynamics, structure, control, fuse, engine ignition, and damage encountered by aircraft at high speeds and in large-overload environments [1–7]. In a hypersonic rocket sled test, a solid rocket engine is used as the power source to push the rocket sled along a high-precision straight track at a hypersonic speed. Simultaneously, the performance parameters of the test products fixed on the sled are tested and analysed using various electronic equipment. Rocket sled systems are widely used in performance tests and reliability assessments of hypersonic vehicles because their carrying capacity, moving velocity, acceleration, and environment are easy to control, and it is easy to observe and collect test data.

A monorail rocket sled is one of the widely used forms of hypersonic rocket sleds. Compared to a duo-rail rocket sled, a monorail rocket sled has much less mass and aerodynamic drag, making it easier to accelerate. However, at the same time, the vibration acceleration of a monorail rocket sled is greater, the stability is poorer, and the mechanical environment is worse. The sled experiences track irregularities, large dynamic loads caused by continuous slipper-track collisions, powerful shock waves, and engine thrust oscillations. These factors cause severe

vibration of the rocket sled system and cause its moving environment to deteriorate sharply [8]. When reaching a hypersonic speed, even a small excitation will cause the rocket sled to vibrate strongly and significantly affect its motion stability. The instability of a rocket sled may result in the failure of the slipper or a track shear fracture and lead to test failure. The dynamic response of a rocket sled directly affects the test environment of the tested product and determines the accuracy and reliability of the test results. Therefore, it is necessary to establish an accurate rocket sled system dynamic model and to analyse its dynamic response.

Some studies have been conducted on the dynamic response of rocket sleds. The earlier methods for predicting the dynamic response of rocket sleds include the empirical coefficient λ method and the sled impact parameter method. Thereafter, some scholars used the finite element method (FEM) to carry out structural response analysis of rocket sleds [9–11]. However, these methods only studied the dynamic response of a rocket sled at a certain speed. In fact, the dynamic characteristics of a rocket sled system vary with the mass, gap between the slipper and track, aerodynamic loads, and thrust. For instance, the fuel consumption will result in a continuous and significant mass reduction for a few seconds and induce a difference in the dynamic response of the rocket sled. Therefore, it is necessary to study the dynamic response of rocket sleds over the entire test period. Generally, the multi-body dynamics method is often used to study the dynamics of the entire test period. According to the initial conditions and boundary conditions of a system, the dynamic differential equations of the system can be solved using this method, and various nonlinear factors can be considered. For a hypersonic rocket sled, its nonlinear factors include aerodynamics, boundary conditions, and slipper–track contact. First, a rocket sled runs from low to hypersonic speeds. In contrast to free flight, the aerodynamic coefficient of a rocket sled changes with velocity owing to the influence of the ground effect and other factors and results in the nonlinear aerodynamic characteristics of the sled. Second, a rocket sled runs along a track with a time-varying gap height between the slipper and track which introduces nonlinearity into the boundary condition. The height of the gap depends on the local track irregularities. In addition, because there is no lubrication between the slipper and the track, it leads to a dry sliding friction phenomenon. Combined with the large impact force generated at high speed and with large loads, the slipper and track undergo very serious wear damage [12], thus increasing the slipper–track gap. These two reasons lead to the discontinuity and nonlinearity of the boundary conditions between the slipper and the track. Third, there are intermittent collisions between the slipper and track during the movement of a rocket sled that introduce nonlinearity into the contact. The normal contact force is a strong nonlinear force related to deformation. In addition, the friction

coefficient of the material surface changes with the sliding velocity after a large number of experiments [13]. Therefore, the tangential contact force also exhibits nonlinear characteristics with a change in the friction coefficient between the slipper and the track.

In summary, the dynamic response of a hypersonic rocket sled is a highly nonlinear dynamic response of a time-varying system. The time-varying and nonlinear factors of the system must be considered to improve the accuracy of research results. Hoose [14-15] considered track irregularity and slipper–track contact force in a study of rocket sled dynamics but did not consider the aerodynamic load on the rocket sled or the influence of slipper–track friction and wear. Wang [16] established a sled–track coupling dynamic model by considering the track irregularities, aerodynamic load, slipper–track contact force, and time-varying characteristics. The acceleration, velocity, displacement, and contact force of the rocket sled system were obtained by numerical calculations, but the influence of slipper–track friction and wear was not considered. Zhang [17] established a multi-body dynamic model of a rocket sled system, considered track irregularities and aerodynamic drag, and analysed the model using the co-simulation method. However, the effects of aerodynamic lift, aerodynamic moment, time-varying mass, friction, and wear were not considered. Gu [18] established a simplified dynamic model of a duo-rail rocket sled system and solved the dynamic equations by considering track irregularities. However, they did not consider the aerodynamic load, time-varying mass, or the influence of friction and wear. In summary, some nonlinear factors have been considered in the study of rocket sled dynamics, but the contact nonlinearity caused by friction and the boundary nonlinearity caused by wear have not been considered. Friction and wear are very important factors for accurately predicting the dynamic response of rocket sleds, because the frictional force affects the prediction of the sliding displacement and sliding velocity of the rocket sled, and the wear of the slipper leads to a change in the slipper–track gap and significantly influences the vertical and lateral acceleration of a rocket sled [19].

Therefore, the influence of slipper–track friction and wear is considered in this dynamic study. A multi-body dynamics research method for a hypersonic rocket sled system combined with friction and wear analysis was established, and the feasibility of the method was verified by comparing the computational results with the rocket sled test results. The time-varying and nonlinear dynamic responses of the hypersonic rocket sled considering friction and wear were obtained and may benefit the design of hypersonic rocket sled systems.

II. Theoretical method

A. Dynamic equations of rocket sled system

The forces and constraints of the monorail hypersonic rocket sled system are shown in Fig. 1. The gravity ***G***, aerodynamic lift ***L***, aerodynamic drag ***D***, and aerodynamic pitching moment $\boldsymbol{M}_p$ act on the centre of mass of the rocket sled when it slides along the track at velocity ***v***. Thrust ***T*** is applied to the engine at the rear of the rocket sled. Three slippers were connected to the rocket sled shell with a fixed joint and were affected by the contact force of the track, including the normal contact force $\boldsymbol{F}_{jn}$ and the frictional force $\boldsymbol{F}_{jt}$ (j = 1, 2, 3). The lower surface of the track was fixed. As shown in Fig. 1, all the forces and moments on the rocket sled varied with time. Owing to fuel consumption, the mass m and the moment of inertia J of the rocket sled were also functions of time t.

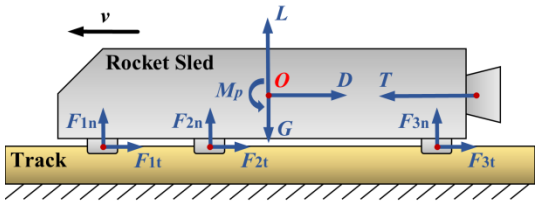

Fig. 1 Forces and constraints of rocket sled system

The Lagrange multiplier method was used to establish dynamic equations according to the force and constraint conditions of the rocket sled system. The Lagrange multiplier method is a relative coordinate method; compared with the Cartesian method, it uses fewer equations. The established dynamic equations are index-3 differential algebraic equations expressed as

$$\begin{pmatrix} \mathbf{M}(\mathbf{q},t) & \boldsymbol{\Phi}_q^{\,T}(\mathbf{q},t) \\ \boldsymbol{\Phi}_q(\mathbf{q},t) & 0 \end{pmatrix} \begin{pmatrix} \ddot{\mathbf{q}} \\ \lambda \end{pmatrix} = \begin{pmatrix} \mathbf{F}(\mathbf{q},\dot{\mathbf{q}},t) \\ \gamma(\mathbf{q},\dot{\mathbf{q}},t) \end{pmatrix}, \tag{1}$$

where $\mathbf{M}$ is the mass matrix, $\boldsymbol{\Phi}_q$ is the Jacobian matrix of the constraint equations, $\ddot{\mathbf{q}}$ is the acceleration, $\dot{\mathbf{q}}$ is the velocity, $\mathbf{q}$ is the generalised coordinates, λ is the Lagrange multiplier, $\mathbf{F}$ is the applied force, and γ is the second-order derivative term in the acceleration equations.

The system is completely constrained, and the constraint equation is

$$\boldsymbol{\Phi}(\mathbf{q},t) = 0\,. \tag{2}$$

The Jacobian matrix $\boldsymbol{\Phi}_q$ of the constraint equation was obtained by solving the partial differential of the constraint equation with respect to the generalised coordinates $\mathbf{q}$ as

$$\boldsymbol{\Phi}_q(\mathbf{q},t)=\frac{\partial\boldsymbol{\Phi}(\mathbf{q},t)}{\partial\mathbf{q}}. \tag{3}$$

The velocity constraint equation was obtained by taking the total differential of Equation (2) with respect to time t as

$$\boldsymbol{\Phi}_q(\mathbf{q},t)\dot{\mathbf{q}}+\boldsymbol{\Phi}_t(\mathbf{q},t)=0. \tag{4}$$

The acceleration constraint equation was obtained by taking the total differential of Equation (4) with respect to time t as

$$\boldsymbol{\Phi}_q\ddot{\mathbf{q}}+(\boldsymbol{\Phi}_q\dot{\mathbf{q}})_q\dot{\mathbf{q}}+2\boldsymbol{\Phi}_{qt}\dot{\mathbf{q}}+\boldsymbol{\Phi}_{tt}=0. \tag{5}$$

The expression of γ obtained from Equation (5) is

$$\gamma=-(\boldsymbol{\Phi}_q\dot{\mathbf{q}})_q\dot{\mathbf{q}}-2\boldsymbol{\Phi}_{qt}\dot{\mathbf{q}}-\boldsymbol{\Phi}_{tt}. \tag{6}$$

The rocket sled system was dominated by the collision contact process. The slide and collision contact between the slipper and track affected each other during the movement of the rocket sled, and the contact load varied with time and the attitude angle of the rocket sled. Therefore, this is a typical dynamic contact problem. Because the slipper–track contact force directly affected the dynamics, friction, and wear characteristics of the rocket sled, it was necessary to establish a reasonable slipper–track contact model. For the slipper–track normal contact force, the L-N nonlinear contact force model was adopted [20]. Compared with the linear contact and Hertz contact models, this model is more suitable for high-speed collision contact problems [21]. The L-N nonlinear contact force model divides the normal contact force $\boldsymbol{F}_n$ into elastic force and damping force as

$$\boldsymbol{F}_n=\max[Kg^e+step(g,DMAX)c\dot{g},0]\boldsymbol{n}, \tag{7}$$

where $\boldsymbol{n}$ is the normal unit vector, K is the contact stiffness, g is the current amount of penetration, $\dot{g}$ is the current relative penetration velocity, e is the exponent, c is the damping constant, *DMAX* is the maximum penetration depth at which the damping force is scaled to $c\dot{g}$ with a cubic step function, and *step*(g,*DMAX*) is a cubic step function that smoothly increases the damping constant from zero to c as the penetration increases from zero to *DMAX*.

According to Equation (7), normal contact force is a strong nonlinear force depending on the amount of penetration. In the L-N nonlinear contact force model, when the amount of penetration g reaches the maximum penetration depth *DMAX*, the two components begin to separate. In a specific rocket sled dynamics computation,

each contact parameter can be calculated using the FEM [16]. The slipper–track tangential contact force (frictional force) $\mathbf{F}_t$ is expressed as

$$\boldsymbol{F}_t = \boldsymbol{F}_n \mu \boldsymbol{n}_\perp , \tag{8}$$

where $\boldsymbol{n}_\perp$ is the tangential unit vector and μ is the kinetic friction coefficient.

B. Friction and wear theory

The stress field of the slipper and track contact was studied in the FEM analysis of the slipper–track friction and wear. There are three main methods of study: displacement, force, and mixed methods. Among them, the displacement method has a clear relationship between the basic variables and is convenient for matrix calculations [22]. Therefore, the displacement method was chosen to study the stress field.

In friction and wear theory, the general parameters used to evaluate the performance of friction and wear are the wear height *h*, wear rate *w*, and *PV* value. The wear height *h* is used to reflect the wear amount, and the wear rate *w* is defined as the ratio of the wear height *h* to the sliding displacement s_x [23]. Because the slipper–track normal pressure *P* and the sliding velocity v_x constitute the independent variables in the calculation of friction and wear, the *PV* value is defined as the product of the two. The normal pressure *P* is the ratio of the normal contact force F_n to the slipper–track contact area *A*.

It is necessary to select the material failure criteria to determine whether the material is worn. Ductile and shear criteria can be used for fracture ductile metals. Ductile fracture is caused by the nucleation and aggregation of microstructural cavities, while shear fracture is caused by the movement of a shear zone. Because measuring fracture strain under different stress triaxialities requires many experiments, to avoid this, Hooputra [24] proposed failure models of ductile fracture and shear fracture. For ductile fracture, the relationship between the equivalent fracture strain ε_D^{**} and stress triaxiality η is

$$\varepsilon_D^{**} = \frac{\varepsilon_T^+ \sinh\left[b\left(\eta^- - \eta\right)\right] + \varepsilon_T^- \sinh\left[b\left(\eta - \eta^+\right)\right]}{\sinh\left[b\left(\eta^- - \eta^+\right)\right]}, \tag{9}$$

where ε_T^+ and ε_T^- are the equivalent plastic strain in equibiaxial tension and compression at ductile fracture, respectively; η^+ and η^- are the stress triaxiality in equibiaxial tension and compression at ductile fracture, respectively; and b is the directionally dependent material parameter in the ductile fracture curve.

When Equation (10) is established, ductile fracture begins to occur.

$$\int_0^{\varepsilon_D^{**}} \frac{d\varepsilon_D}{\varepsilon_D^{**}(\eta)} = 1 \tag{10}$$

For shear fracture, the shear stress parameter θ is defined as

$$\theta = \frac{1 - k_S \eta}{\phi}, \tag{11}$$

where k_S is the material parameter in the shear fracture curve, and ϕ is the ratio of the maximum shear stress to the equivalent stress. Then, the relationship between the equivalent fracture strain ε_S^{**} and the shear stress parameter θ is

$$\varepsilon_S^{**} = \frac{\varepsilon_S^{+} \sinh\left[f\left(\theta - \theta^{-}\right)\right] + \varepsilon_S^{-} \sinh\left[f\left(\theta^{+} - \theta\right)\right]}{\sinh\left[f\left(\theta^{+} - \theta^{-}\right)\right]}, \tag{12}$$

where ε_S^{+} and ε_S^{-} are the equivalent plastic strain in equibiaxial tension and compression at shear fracture, respectively; f is the material parameter in the shear fracture curve; and θ^{+} and θ^{-} are the shear stress parameters for equibiaxial tension and compression, respectively.

$$\begin{aligned} \theta^{+} &= 2 - 4k_S \\ \theta^{-} &= 2 + 4k_S \end{aligned} \tag{13}$$

When Equation (14) is established, shear fracture begins to occur.

$$\int_0^{\varepsilon_S^{**}} \frac{d\varepsilon_S}{\varepsilon_S^{**}(\theta)} = 1 \tag{14}$$

According to the above material failure criteria, it can be determined whether the slipper material has ductile or shear fracture through the FEM calculation, and then the slipper wear can be determined.

III. Computational method

A. Dynamics analysis method

1. Dynamic model

The first step of the multi-body dynamics computation of a rocket sled system is to establish the model of the rocket sled and track. The monorail rocket sled used in this test adopted a three-stage tandem propulsion as shown in Fig. 2. During the movement of the rocket sled, the second-stage sled engine worked at t_1 after the first-stage sled

engine finishes working, and then the first-stage sled separated. Similarly, the third-stage sled engine worked at t_2 after the second-stage sled engine finished working, and then the second-stage sled separated. The third-stage sled finally reached hypersonic speed, which was the simulation object.

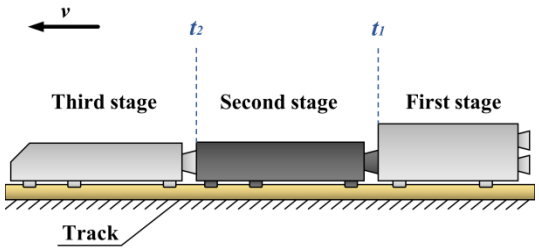

Fig. 2 Three-stage rocket sled

The third-stage sled contained a sled body and propellant. The sled body contained the shell, internal structure, test product, engine, electronic equipment, and three slippers. The test product was integrated into the third-stage sled. The initial mass of the third-stage sled was 894 kg. The time-varying curve of the mass characteristics of the third-stage sled propellant was obtained according to the factory parameters of the solid rocket engine as shown in Fig. 3. Since the propellant was of a rotating shape and burnt from the inside out, the yaw moment of inertia curve was the same as the pitch moment of inertia curve. It was found that the reduction rates of mass, yaw moment of inertia, and pitch moment of inertia remained constant after t_2 = 6.166 s, while the roll moment of inertia showed nonlinear time-varying characteristics. The initial propellant mass in the third-stage sled accounted for approximately 42.8% of the total mass and lost within 9.475 s, indicating that the rocket sled system had strong time-varying mass characteristics.

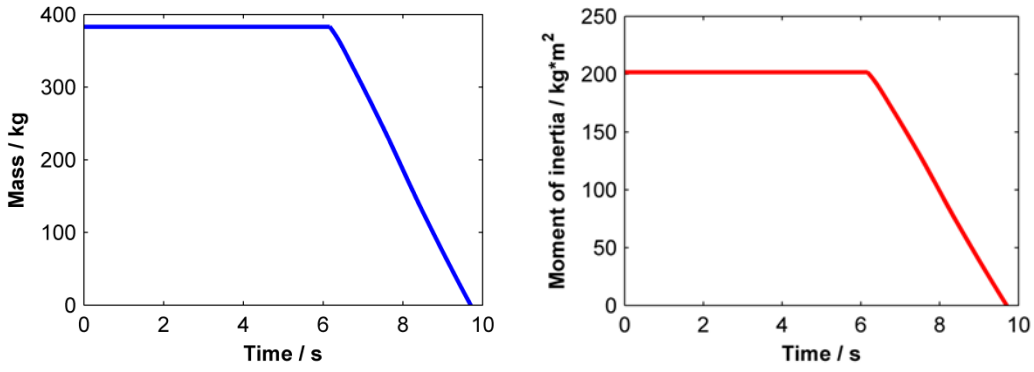

(a) mass **(b) yaw moment of inertia**

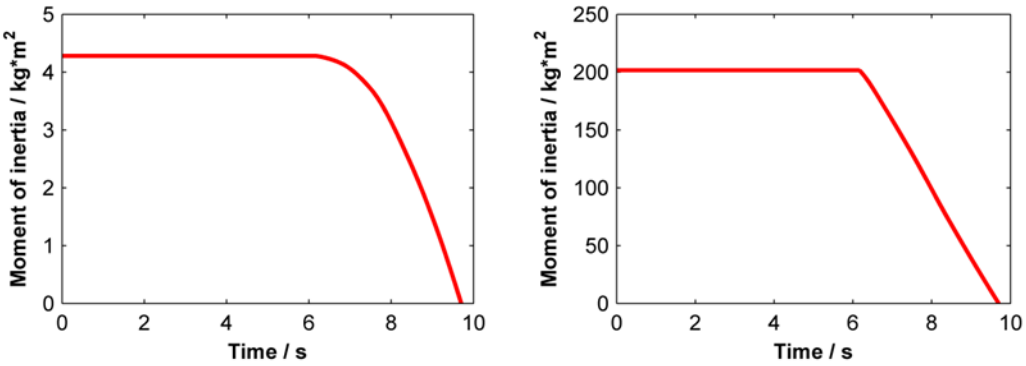

(c) roll moment of inertia **(d) pitch moment of inertia**

Fig. 3 Time-varying mass characteristics of propellant

Track irregularity is one of the main factors causing the vibration of a rocket sled; therefore, the vertical irregularity was measured by an optical method. Considering the measurement error, the original information obtained from the measurement was detrended to obtain the vertical track spectrum as shown in Fig. 4. Because the computational method mainly focused on the vertical track spectrum, the lateral track spectrum was not established, and the subsequent analysis was limited to the vertical direction.

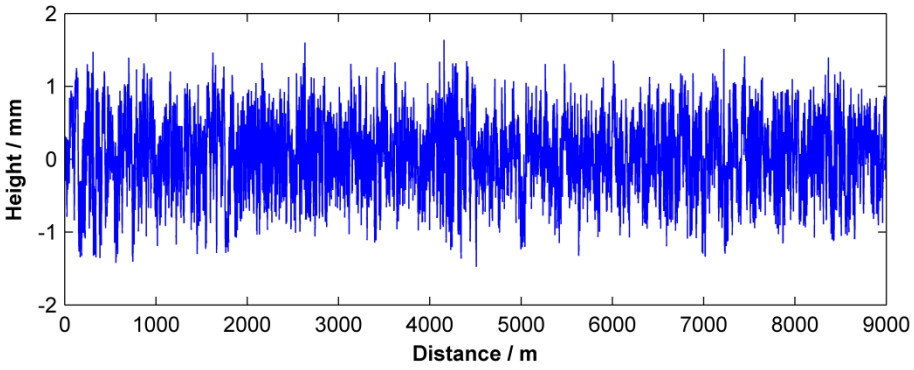

Fig. 4 Vertical track spectrum

According to the vertical track spectrum shown in Fig. 4, a track model with irregularities was established. The third-stage sled model was assembled using the track model shown in Fig. 5. An initial 1.9-mm gap was found between the slipper and the track, and the gap varied with the local track spectrum.

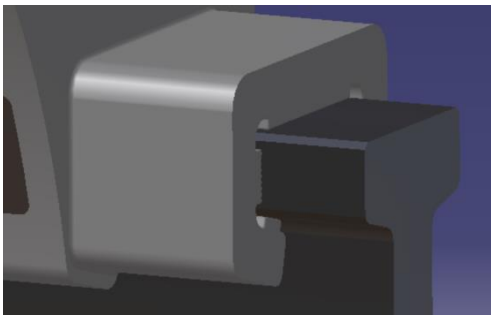

Fig. 5 Assembly of slipper and track

2. Sled loads

The second step of the multi-body dynamics computation of the rocket sled system was to calculate the load characteristics, including the thrust for the entire period and the aerodynamic load at different velocities, and use them as the input conditions for the dynamics computation. In the process of the multi-body dynamics computation of the rocket sled system, the position and direction of thrust and aerodynamic loads are shown in Fig. 1. The eccentricities of thrust and aerodynamic drag were not considered.

As for the thrust calculation, because the research object was the third-stage sled, the thrust curve after time t_2 of the third-stage sled engine provided by the factory was used directly. The force of the second-stage sled on the third-stage sled was used as the equivalent thrust curve before time t_2. The calculated third-stage sled thrust curve for the entire time period is shown in Fig. 6. It was found that the ignition times of the second and third stages were t_1 = 2.379 s and t_2 = 6.166 s, respectively, and the thrust oscillation phenomenon existed in the rocket sled engines.

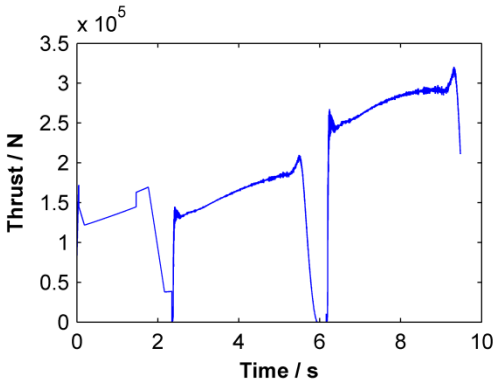

Fig. 6 Thrust curve

The aerodynamic loads of the third-stage sled were obtained using the computational fluid dynamics method. The steady aerodynamic loads of the third-stage sled under different *Ma* were calculated, and the aerodynamic loads at other velocities were obtained by piecewise interpolation and used as the input conditions for the multi-body dynamics computation of the rocket sled system. During the dynamics analysis, the sliding velocity v_x of the third-stage sled was solved at each time step to obtain the corresponding aerodynamic loads at that time step. Owing to the small gap between the slipper and the track, the attitude angle $\boldsymbol{\beta}$ of the rocket sled was limited to a very small range; therefore, the angle of attack and angle of sideslip of the rocket sled were not considered in the aerodynamic calculation. Accordingly, only lift $\boldsymbol{L}$, drag $\boldsymbol{D}$, and pitch moment $\boldsymbol{M}_p$ were considered as aerodynamic loads.

For the aerodynamic calculation of the third-stage sled, steady three-dimensional compressible viscous Navier–Stokes equations were adopted as the governing equations. The spatial difference format was the Roe format [25], and the non-physical solution was modified using the entropy method. The Roe format is one of the most successful upwind formats in practical applications because of its excellent viscous resolution and shock wave discontinuous resolution. The lower-upper symmetric Gauss–Seidel (LU-SGS) implicit time stepping format [26] was used, which has the characteristics of small computation requirements and good robustness. The turbulence was solved using the Reynolds-averaged Navier–Stokes method, and the two-equation realised k-ε turbulence model was used. The length of the third-stage sled was denoted as H, and the flow field was set as a cuboid, with a length, width, and height of 10H, 5H, and 5H, respectively. The inlet and far field of the flow field were set as far-field boundaries. The outlet was set as a supersonic outlet boundary. And the sled was set as a non-slip adiabatic wall. The track and the ground were set as translational walls, whose translational speed was consistent with the incoming flow speed. Considering the ground effect and symmetry of the structure, the 1/2 flow field grid model was established as shown in Fig. 7.

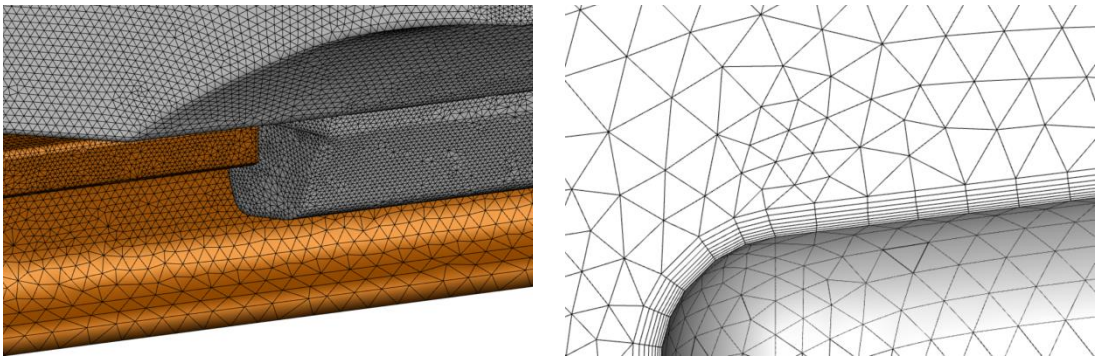

(a) Local grid **(b) Boundary-layer grid**

Fig. 7 Flow field grid model

The aerodynamic load curves of the third-stage sled after the calculation are shown in Fig. 8. The centre of the pitch moment $\boldsymbol{M}_p$ was the centre of mass of the third-stage sled. When the pitch moment $\boldsymbol{M}_p$ was positive, it was a pitch-down moment. As can be seen, the lift $\boldsymbol{L}$, drag $\boldsymbol{D}$, and pitch moment $\boldsymbol{M}_p$ were not proportional to Ma^2 within the range of Ma = 0–6, indicating that the aerodynamic coefficients constantly varied with velocity, thus reflecting the nonlinear aerodynamic characteristics of the rocket sled.

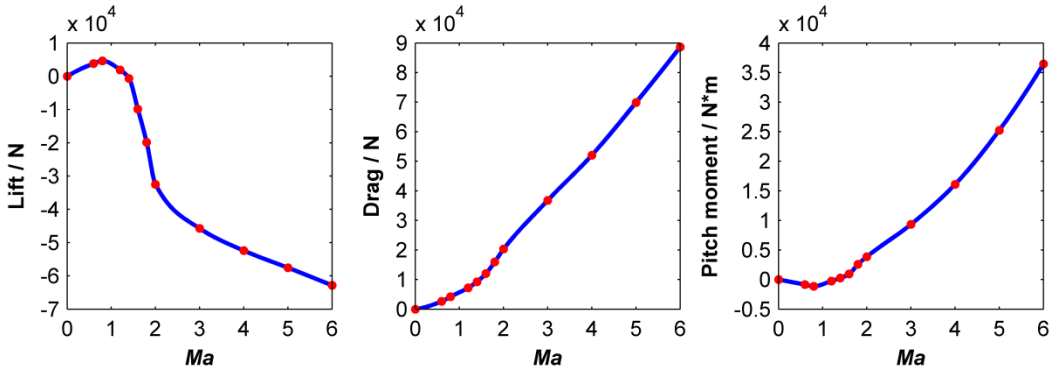

Fig. 8 Aerodynamic load curves

3. Dynamics analysis method

First, a multi-body dynamics simulation of a hypersonic rocket sled system was carried out without considering friction and wear. The computational process is illustrated in Fig. 9. The time-varying propellant mass curves, thrust curve, and aerodynamic load curves were introduced to obtain the mass matrix $\mathbf{M}$, engine thrust $\boldsymbol{T}$, and aerodynamic loads at different time steps when initialising the dynamic model. To solve the contact force, the local track spectrum heights and slopes of the three slippers were obtained according to the sliding displacement s_x of the third-stage sled. It was then determined whether the three slippers were in contact with the track, so the vertical displacements s_y, lateral displacements s_z, and attitude angles $\boldsymbol{\beta}$ of the three slippers were calculated. If there was no contact, there was no contact force at this time step; if there was contact, then the current penetration depth g was obtained. The current relative penetration velocity $\dot{g}$ was obtained according to the local track spectrum slope, vertical velocity v_y, and lateral velocity v_z of the slipper. According to Equations (7) and (8), the slipper–track normal contact force $\boldsymbol{F_n}$ and frictional force $\boldsymbol{F_t}$ were obtained, in which the kinetic friction coefficient μ = 0.2 was defined.

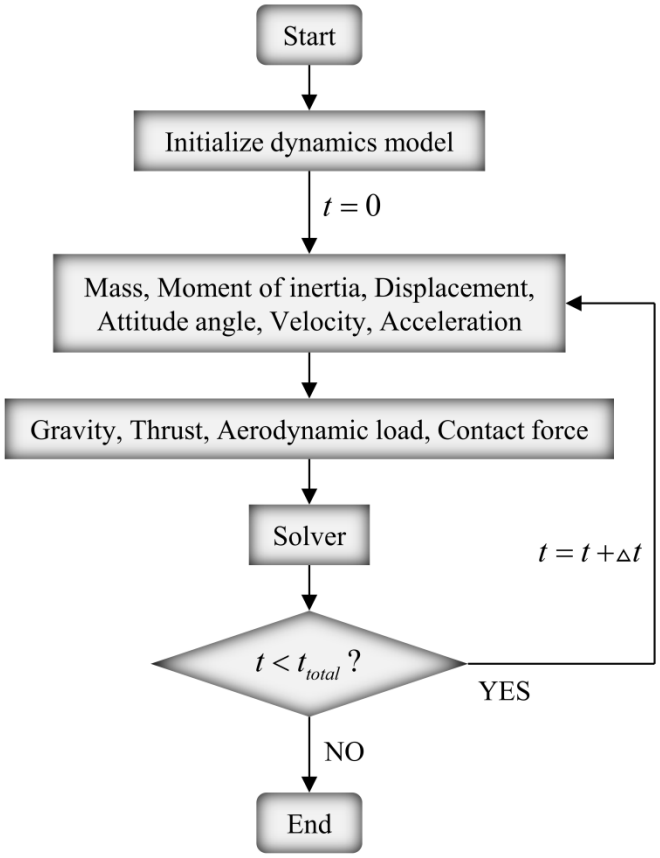

Fig. 9 Dynamics computational process without considering friction and wear

The multi-body dynamics calculation of the rocket sled system was based on the commercial software LMS Virtual.Lab Motion. To solve the dynamic equations, a sparse matrix was used to improve the operation speed. The integration algorithm used was the backward differentiation formula (BDF) [27], which is an implicit multi-step integration algorithm with variable order and variable step size. The advantage of the BDF is that it is inherently stable for stiff systems. The ordinary differential equations in multi-body dynamics are second-order, and the basic form is

$$\ddot{\mathbf{q}} = f\left(\mathbf{q}, \dot{\mathbf{q}}, t\right). \tag{15}$$

The BDF method was used to iteratively solve Equation (15) so that the equation converged at each time step. The iteration format was

$$\begin{cases} \mathbf{q}_{n+1} = l\varphi_k \dot{\mathbf{q}}_{n+1} + \sum_{i=1-k}^{0} \psi_i \mathbf{q}_{n+i} \\ \dot{\mathbf{q}}_{n+1} = l\varphi_k f_{n+1} + \sum_{i=1-k}^{0} \psi_i \dot{\mathbf{q}}_{n+i} \end{cases}, \tag{16}$$

where ψ_i and φ_k are the coefficients, and l is the step size. For rigid ordinary differential equations, the range of k was $1 \le k \le 6$, and the resolution of the k-step method was of the order k. In Equation (16), velocity and f_{n+1} must be predicted. f_{n+1} is a function of the velocity and generalised coordinate at time $n + 1$.

$$f_{n+1} = f_{n+1}(\mathbf{q}_{n+1}, \dot{\mathbf{q}}_{n+1}) \tag{17}$$

For the calculation of acceleration, the matrix was simplified to a banded matrix as much as possible, and the matrix was factored to reduce the operation time. The total calculation time t_{total} was 9.475 s and defined as the maximum time of the thrust curve.

A multi-body dynamics simulation considering the friction and wear of the hypersonic rocket sled system was also carried out. The computational process was illustrated in Fig. 10. According to the case without considering friction and wear, the sliding displacement $s_x(t)$, sliding velocity $v_x(t)$, and slipper–track normal contact force $F_n(t)$ over the entire time period were output as the input conditions for the friction and wear computation. Then, the kinetic friction coefficient $\mu(PV)$ curve and the wear height $h(s_x)$ curve were output as the input conditions for the dynamics computation considering friction and wear. The wear height h of the slipper increased with an increase in the sliding displacement s_x. However, it was unrealistic to change the shape of the slipper at each time step in the rocket sled dynamics computation. In fact, the continuous wear of the slipper was reflected in the rocket sled dynamics as the gap between the slipper and track increased. Therefore, although the shape of the slipper was not adjusted during the modelling, the shape of the track was adjusted to make the slipper–track gap at each point on the track reflect the wear height of the slipper at that point. Because the size of the gap was very small relative to the slipper and track, this equivalent method was reasonable. Therefore, the track was remodelled by combining the vertical track spectrum and the wear height $h(s_x)$ curve in the dynamic analysis considering friction and wear. In contrast to the computational process shown in Fig. 9, the kinetic friction coefficient $\mu(PV)$ curve and the worn-track model needed to be imported during the initialisation of the computational process shown in Fig. 10. To calculate the slipper–track frictional force $\boldsymbol{F_t}$, the normal pressure P was obtained by dividing the normal contact force $\boldsymbol{F_n}$ by the contact area A = 0.02 m^2. The kinetic friction coefficient μ corresponding to the normal pressure P and the sliding velocity v_x was obtained according to the kinetic friction coefficient $\mu(PV)$ curve, and the slipper–track frictional force $\boldsymbol{F_t}$ was obtained according to Equation (8).

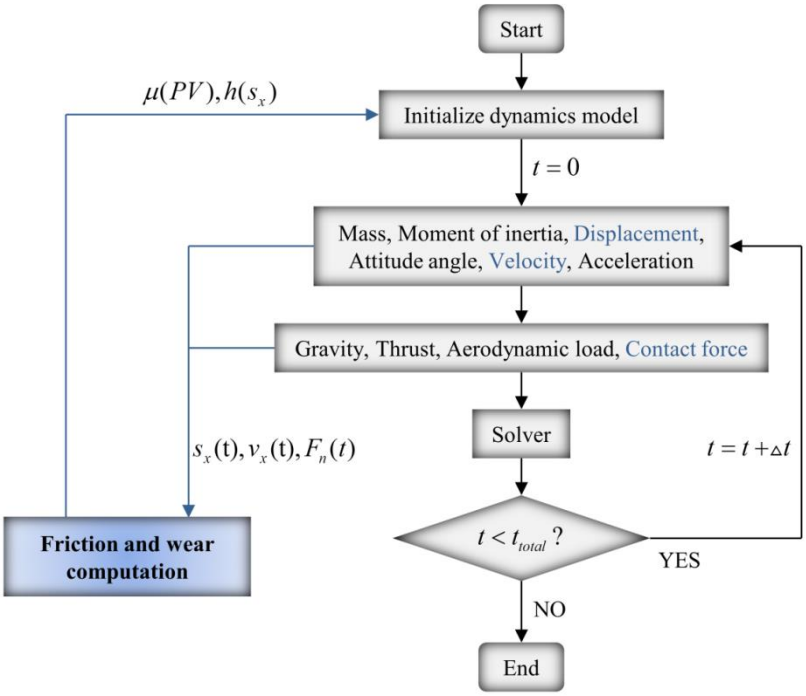

Fig. 10 Dynamics computation process considering friction and wear

B. Friction and wear computation

The kinetic friction coefficient was computed using the method presented in Ref. [28]. First, the actual surface roughness of the slipper and track was measured, and the W-M function method [29] was used to establish a rough surface profile. The W-M function method has a clear parameter meaning and high accuracy and is widely used. A finite element model with a rough surface was created based on the rough surface profile as shown in Fig. 11. The left and right ends of the track were set as symmetric constraints to simulate an infinite-length track, and the lower surface of the track was set as a fixed constraint. According to the sliding velocity $v_x(t)$ and normal contact force $F_n(t)$ obtained from the rocket sled dynamics computation, normal pressure P was applied to the upper surface of the slipper, and the sliding velocity v_x was applied to the slipper. The contact mode between the slipper and track was set as hard contact and frictionless. The materials of the slipper and track were 18Ni(300) steel and U71Mn steel, respectively, and their material properties are listed in Table 1. Because the slipper–track collision model is a high-speed collision model, the Johnson–Cook constitutive model was used for computation.

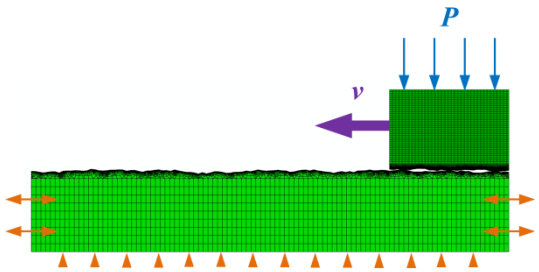

Fig. 11 Slipper–track finite element model with rough surface

Table 1 Slipper–track material properties

Parameter	Slipper	Track
Density / kg·m^{-3}	8000	7920
Elastic modulus / GPa	190	210
Poisson ratio	0.283	0.3

Because the slipper and track contact intermittently, there may be no slipper–track contact at the time of a certain sliding velocity v_x; that is, the normal pressure $P(v_x) = 0$ at that time. Therefore, the root mean square (RMS) values of the non-zero normal pressure P in a small range around each sliding velocity v_x were used to calculate the kinetic friction coefficient under multiple groups of PV values. The shear stress and normal stress of the contact nodes were extracted from the computational results and divided by each other to obtain the kinetic friction coefficients μ under multiple groups of PV values. The kinetic friction coefficient $\mu(PV)$ curve was fitted with multiple groups of data. Then, the $\mu(PV)$ curve was used as the input condition for the multi-body dynamics computation of the rocket sled system considering friction and wear.

In related studies, the friction between the slipper and track was considered to be similar to the collision of small particles. Therefore, a slipper–track microscopic sub-model of the finite element was established, and a single micro-convex was used to represent the roughness of the entire track as shown in Fig. 12. The slipper and track were set to be deformable bodies, and they deformed plastically after contact. All the degrees of freedom at the lower surface of the track were constrained, and the left and right ends of the track were set as symmetric constraints. The initial velocity condition was loaded on each node of the slipper to prevent grid distortion. The subsequent velocity boundary conditions were applied to the upper and right surfaces of the slipper to make the slipper deformable. Because the normal pressure P corresponds to the sliding velocity v_x, the load was not applied to the upper surface of the slipper. Instead, the vertical and rotational degrees of freedom on the upper surface of the slipper were set to zero, and the sliding velocity v_x was used to replace the PV value to carry out multiple groups of wear computations.

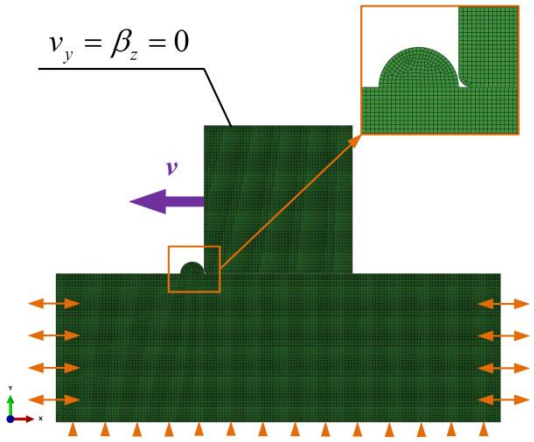

Fig. 12 Slipper–track microscopic sub-model

Both the slipper and track were worn during the wear computation. However, the track after wear did not affect the motion of the rocket sled; therefore, the wear computation only focused on the slipper. Combined with the element stress generated by computation and the failure criteria shown in Equations (9)–(14), the number of slipper failure elements at the computational sliding velocity v_x was determined. By counting the number of failure elements at each computational sliding velocity v_x, the wear rate w at each computational sliding velocity v_x was obtained. Combined with the relationship between the sliding displacement $s_x(t)$ and the sliding velocity $v_x(t)$ obtained from the rocket sled dynamics computation, the wear rate w of each computational sliding displacement s_x was obtained, and the wear rate $w(s_x)$ curve was obtained through interpolation. By integrating the wear rate $w(s_x)$ before each sliding displacement s_x, the wear height $h(s_x)$ curve of the slipper was obtained. The wear height $h(s_x)$ curve was superimposed with the vertical track spectrum, and then the track model including the track spectrum considering wear was established. The newly established track model was the input condition for the multi-body dynamics computation of the rocket sled system considering friction and wear.

IV. Hypersonic rocket sled test

A hypersonic rocket sled test was carried out to verify the computational method of the hypersonic rocket sled dynamic response considering friction and wear. The test system was mainly composed of a rocket sled, track, sled-mounted test equipment, and ground test equipment as shown in Fig. 13. The sled-mounted test equipment was installed inside the sled, including the acceleration sensor, storage system, power system, telemetry equipment, and synchronous trigger. The ground test equipment mainly included a ground telemetry receiver, velocity radar, and photoelectric theodolite.

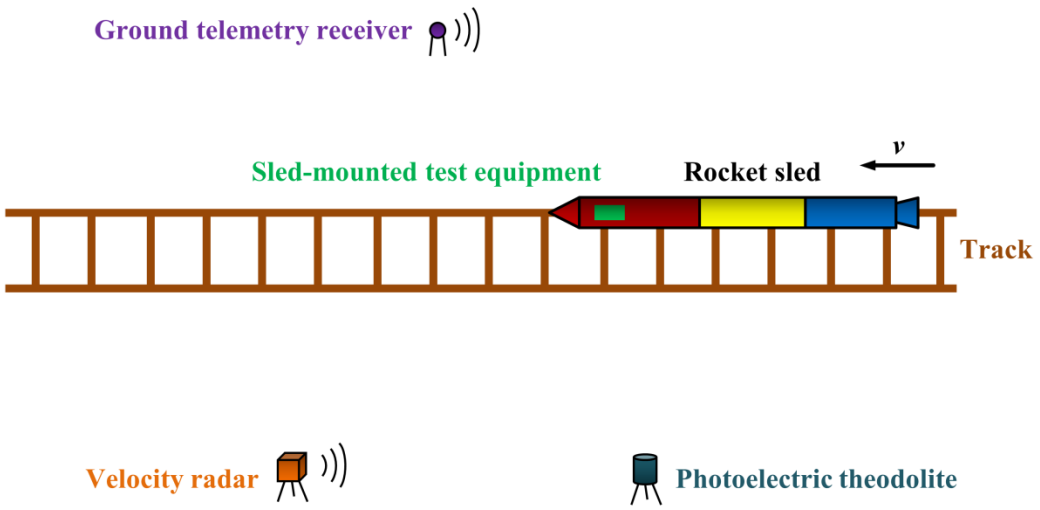

Fig. 13 Rocket sled test system

The photoelectric theodolite is a high-precision measuring device with a tracking function that can realise automatic tracking and high-speed photography of a rocket sled. The velocity of the rocket sled was measured using velocity radar. An acceleration sensor was installed at the front slipper of the third-stage sled to collect the vibration acceleration signal. For the poor mechanical environment of a hypersonic rocket sled, a small lightweight acceleration sensor with a strong impact resistance and high temperature resistance was selected, and a static and dynamic calibration was performed to ensure test accuracy. The sensor signal was transmitted to the sled-mounted storage system via a cable, and the sled-mounted telemetry equipment transformed the electrical signal into a telemetry signal. The ground telemetry receiver received the wireless telemetry signal and transformed it into an electrical signal in a specified format for real-time display and storage. The test data was instantly transmitted through the telemetry system.

The test used a three-stage tandem-propulsion monorail rocket sled, which was consistent with the computation. When the rocket sled was launched, the trigger signal was generated by the sled-mounted synchronous trigger because of the movement of the rocket sled. The transistor-transistor logic signal was output synchronously to the storage system and telemetry system to ensure that the time zero of each sled-mounted system was unified. When the rocket sled moved along the track, each test system collected the data. The test results revealed that the maximum Mach number of the third-stage sled was 5.2. The ground test equipment recorded the sliding displacement and sliding velocity of the third-stage sled over the entire period. The ground telemetry receiver collected the vibration acceleration data before 7.575 s, but the data after 7.575 s were not collected.

V. Results and analysis

A. Friction and wear analysis

Based on the multi-body dynamics computation of the rocket sled system without considering friction and wear, the sliding displacement $s_x(t)$, sliding velocity $v_x(t)$, and front slipper-track normal contact force $F_n(t)$ of the third-stage sled over the entire time period were obtained. The normal pressure P under different sliding velocities was obtained by combining the front slipper-track normal contact force $F_n(t)$ and sliding velocity $v_x(t)$ as shown in Fig. 14. The maximum sliding displacement of the rocket sled was 6916 m, the maximum sliding velocity of the rocket sled was 1760 m/s, and the maximum slipper–track normal contact force was 2.4×10^5 N during t_{total} = 9.475 s. As shown in Fig. 14(c), the slipper–track normal contact force changed dramatically over the entire period. A positive value indicates that a slipper was in contact with the upper surface of the track and thus was subjected to a vertical upward force. The negative value indicates that a slipper was in contact with the lower surface of the track and thus was subjected to a vertical downward force. The occurrence ratio of positive and negative values was 1.036 according to statistics, and they appeared alternately, indicating that the slipper and track collided back and forth in the vertical direction. As shown in Fig. 14(d), the RMS value of the normal pressure P and the sliding velocity v_x showed a clear positive correlation. The RMS value of the normal pressure P reached a maximum value of 11.954 MPa at Mach 5.

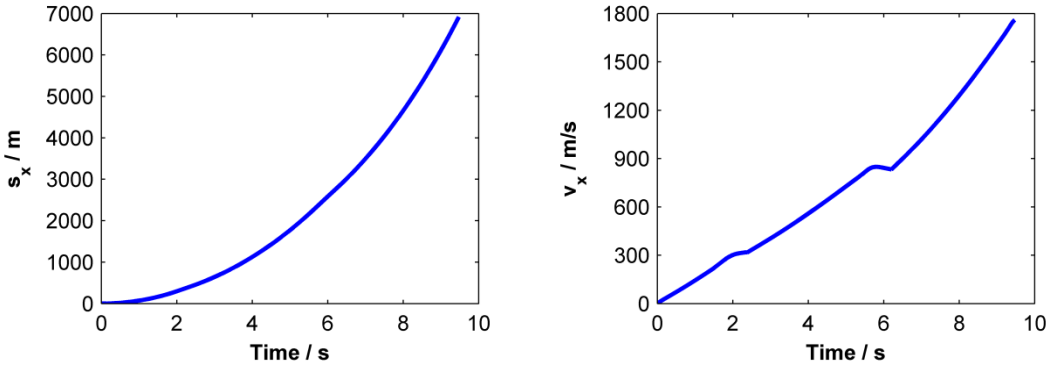

(a) sliding displacement vs. time **(b) sliding velocity vs. time**

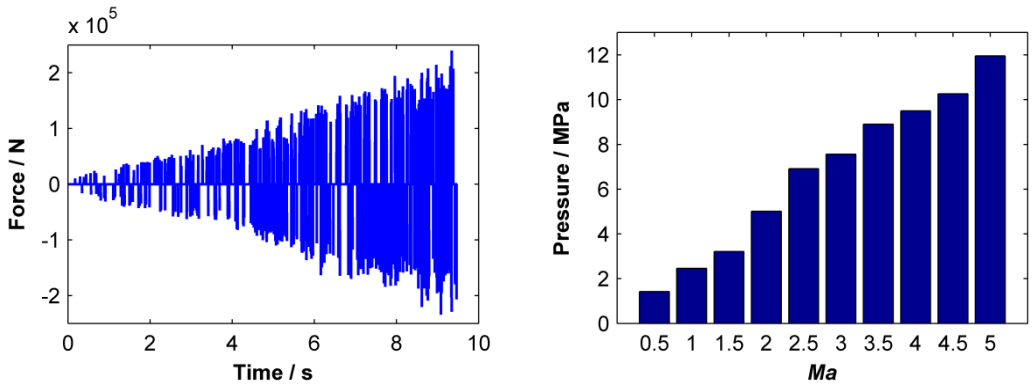

(c) slipper–track normal contact force vs. time **(d) normal pressure vs. sliding velocity**

Fig. 14 Input conditions for friction and wear computation

Under normal pressure P and sliding velocity v_x shown in Fig. 14(d), kinetic friction coefficient computations were carried out to obtain 10 groups of kinetic friction coefficient μ under PV values, which were then fitted into the kinetic friction coefficient $\mu(PV)$ curve shown in Fig. 15. The fitting function was

$$\mu(PV) = 0.1231e^{-0.0003889PV} + 0.2994e^{-0.00001435PV}. \quad (18)$$

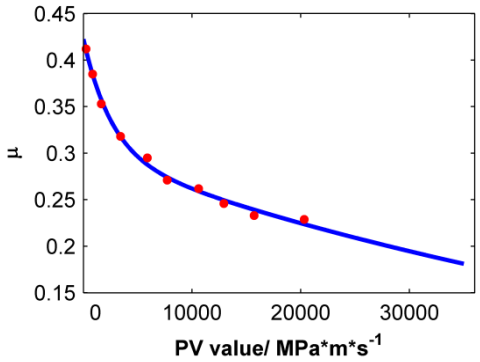

Fig. 15 Kinetic friction coefficient curve

As shown in Fig. 15 and Equation (18), the kinetic friction coefficient μ decreased with an increase in the PV value, and the rate of decrease was high at the beginning and then lowered. Because the kinetic friction coefficient μ changed nonlinearly with the PV value, the frictional force between the slipper and the track showed contact nonlinearity. The wear was calculated at 10 different velocities as shown in Fig. 14(d). The slipper stress distributions at Ma = 1, 3, and 5 are shown in Fig. 16. By comparing the stress distribution at the three velocities, it was found that the stress generated by the slipper increased, and the stress concentration area decreased with an increase in velocity. This is because the stress became more difficult to transfer to other interior areas in a timely manner as the velocity increased, resulting in a stress concentration in the contact area of the slipper and the track micro-convex.

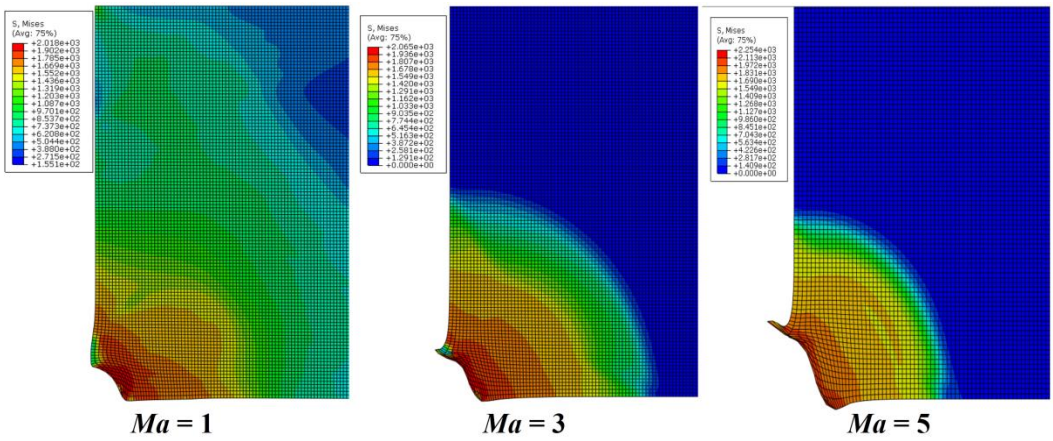

Fig. 16 Slipper stress distribution

In combination with the stress distribution of each working condition and the material failure criteria, the wear rate w of the sliding velocity v_x under each working condition was obtained as shown in Fig. 17. The wear rate w increased with an increase in sliding velocity v_x in the Mach ranges 0.5–2 and 2.5–5. However, the wear rate decreased in the Mach range 2–2.5 because the principal strain rate increased by one order of magnitude within this PV value range, leading to a decrease in the number of elements judged as failure.

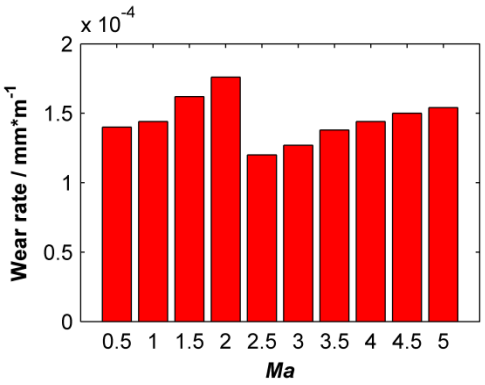

Fig. 17 Slipper wear rate vs. sliding velocity

According to the wear rate $w(v_x)$ of the above sliding velocities, combined with the relationship between the sliding displacement $s_x(t)$ and the sliding velocity $v_x(t)$ in Fig. 14(a) and 14(b), the wear rate w of each computational sliding displacement s_x was obtained. The wear rate $w(s_x)$ curve was obtained through interpolation as shown in Fig. 18. The wear rate $w(s_x)$ was integrated along the sliding displacement s_x to obtain the wear height $h(s_x)$ curve of the slipper as shown in Fig. 19. The wear height h increased almost linearly with the sliding displacement s_x. The maximum sliding displacement obtained by computation was 6916 m, and the corresponding wear height was 0.9875 mm. The above wear height $h(s_x)$ curve was superimposed with the vertical track spectrum in Fig. 4 to obtain the vertical track spectrum considering wear as shown in Fig. 20, and a track model considering wear was

established based on the track spectrum. Because the new track model considered the irregularity and wear, the boundary conditions of the rocket sled slipper at different track positions were different and demonstrated the boundary nonlinearity of the hypersonic rocket sled dynamics.

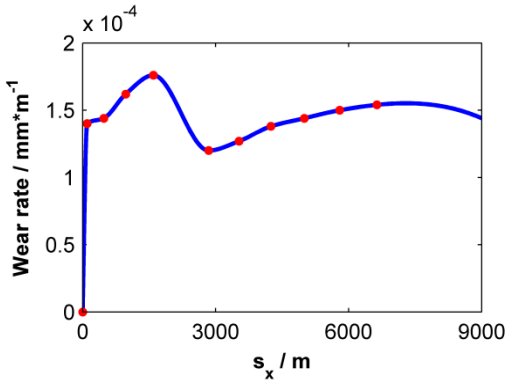

Fig. 18 Slipper wear rate vs. sliding displacement

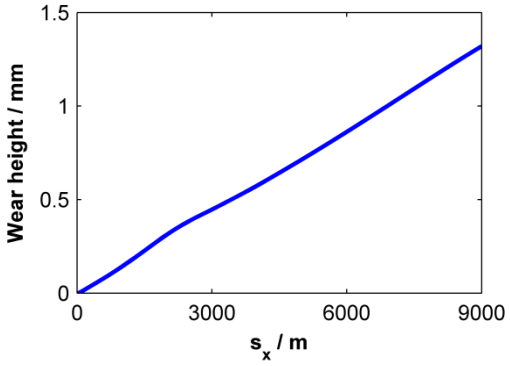

Fig. 19 Slipper wear height vs. sliding displacement

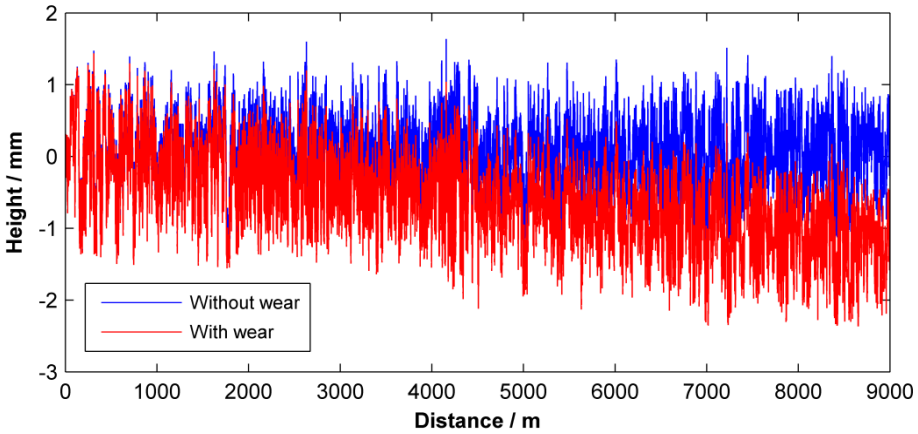

Fig. 20 Vertical track spectrum considering wear

B. Dynamic response analysis

The sliding displacement s_x and sliding velocity v_x curves of the rocket sled over the entire computation and testing period are shown in Fig. 21. The curves of sliding displacement s_x and sliding velocity v_x obtained by computation matched well with the test values, which confirmed the effectiveness of the computational method in the prediction of sliding displacement and velocity. The time at which the third-stage sled reached the maximum sliding velocity was called the total time. After that, the rocket sled gradually slowed down without thrust until it left the end of the track. The total time and maximum values of the sliding displacement and velocity are listed in Table 2. It can be seen from the table that the total test time was 9.328 s, while the total computation time was 9.475 s, with an error of 1.6%. For the sliding displacement, the computational value was larger than the test value. The error between the maximum sliding displacement of the test and the value of the dynamics computation considering friction and wear was 4.7%, and the error between the maximum sliding displacement of the test and the value of the dynamic computation without considering friction and wear was 6.2%. The computational value of the sliding velocity was smaller than that of the test value. The error between the test maximum sliding velocity and that of the dynamic computation considering friction and wear was 1.2%, and the error between the test maximum sliding velocity and that of the dynamic computation without considering friction and wear was 0.6%. As shown in Fig. 21(b), the computation accurately predicted the velocity changes of the rocket sled during the separation of each stage but failed to predict the abnormal velocity changes of the third-stage sled within a short time before the maximum velocity. This abnormal change in velocity may have been caused by the abnormal combustion of the propellant at this time. In addition, the sliding velocity and displacement without considering friction and wear were slightly larger than those considering friction and wear. This is because in the dynamics computation without considering friction and wear, the kinetic friction coefficient was defined as $\mu = 0.2$, which was smaller than the kinetic friction coefficient considering friction and wear at most times. Because the frictional resistance was smaller, the rocket sled moved faster and farther. However, the frictional force was too small compared with the thrust, and the slipper was not in contact with the track at all times; therefore, the sliding displacement and velocity of the two computations were similar. This indicates that within the acceptable error range, it is reasonable to consider dynamic computational results without considering friction and wear as the input to perform friction and wear computations, even if there is a small deviation between the input and the dynamic results considering friction and wear.

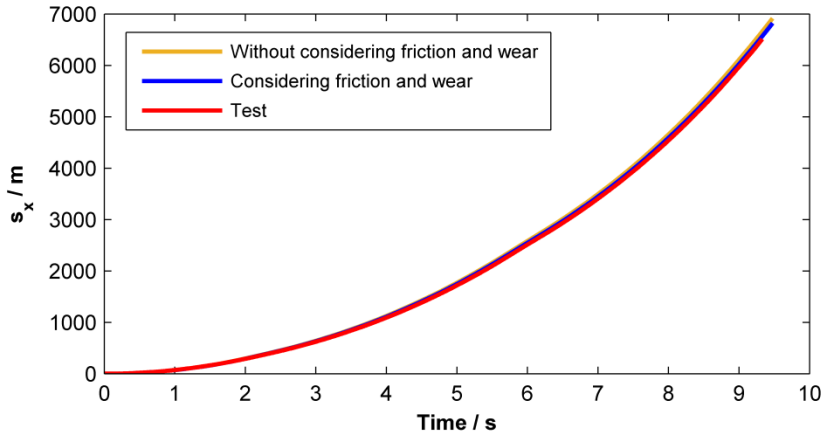

(a) Sliding displacement

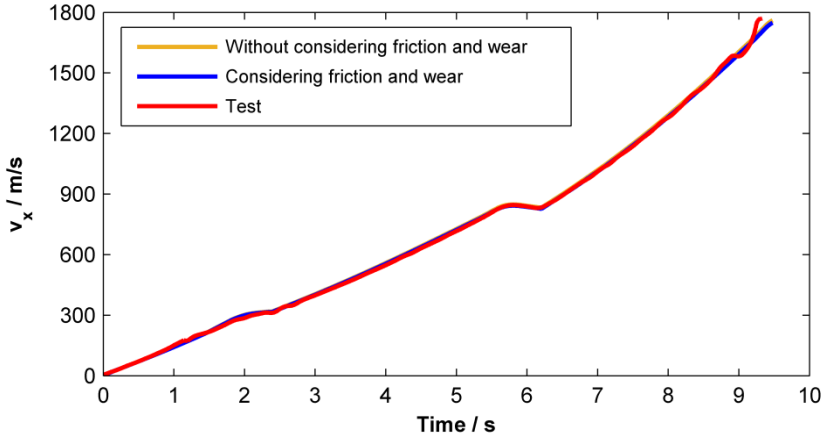

(b) Sliding velocity

Fig. 21 Sliding displacement and velocity of test and computation

Table 2 Total time and maximum values of sliding displacement and velocity

	Without considering friction and wear	Considering friction and wear	Test
Total time / s	9.475	9.475	9.328
Maximum sliding displacement / m	6916	6821	6512
Maximum sliding velocity / m*s^{-1}	1760	1748	1770

Figure 22 shows the curve of the third-stage sled pitch angle β_z over the entire computation period. In the previous analysis, the third-stage sled was mostly subjected to a pitch-down moment. However, Figure 22 shows that the pitch angle of the rocket sled oscillated around 0° without a clear pitch-down phenomenon, indicating that the aerodynamic moment of the third-stage sled was not sufficient to overcome the larger slipper-track contact force.

In the case of considering friction and wear, the amplitude of the pitch angle increased with time owing to the time-varying gap between the slipper and track. In addition, the frequency of the pitch angle fluctuation was higher than that without considering friction and wear. This indicates that wear had a significant influence on the attitude angle of the rocket sled. However, the maximum pitch angle of the rocket sled was less than 0.04°. Therefore, it is reasonable to ignore the influence of the angle of attack on the aerodynamic computation.

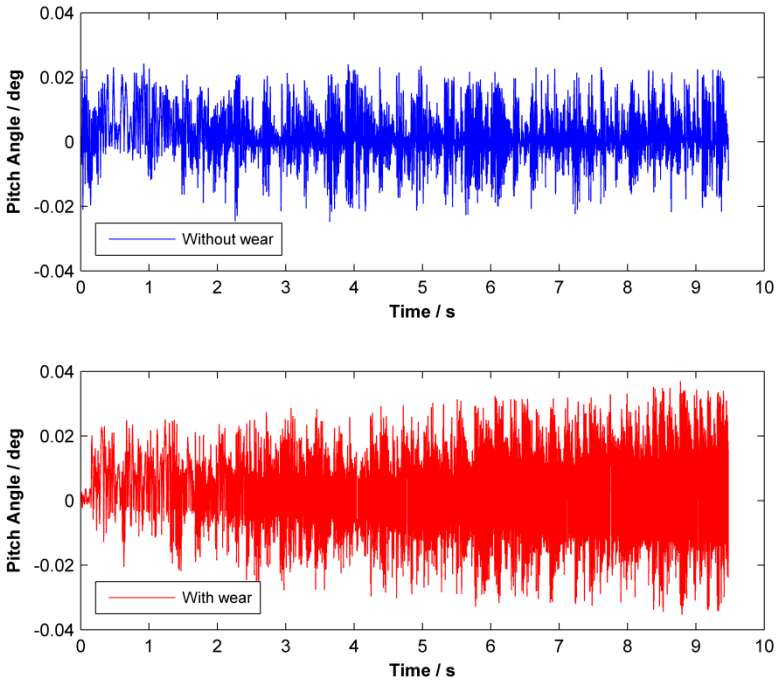

Fig. 22 Pitch angle

The vertical vibration acceleration a_y of the front slipper of the third-stage sled over the entire period is shown in Fig. 23, in which the test data was collected before 7.575 s. The results show that the vertical vibration acceleration of the front slipper was distributed almost symmetrically along the x-axis and changed dramatically. The maximum value reached 360 *g*, indicating a poor rocket sled dynamic environment. The rocket sled was affected by track irregularity, shock wave impact, oscillating engine thrust, and time-varying mass characteristics; therefore, its stability was poor. Once the rocket sled was unstable, a large slipper–track collision occurred, resulting in a large acceleration. As shown in Fig. 23, large vibration accelerations occur occasionally, and this phenomenon occurs more often at high speeds. This indicates that the slipper–track collision frequency was higher at high speeds than at low speeds, which was consistent with the slipper–track contact frequency shown in Fig. 14(c).

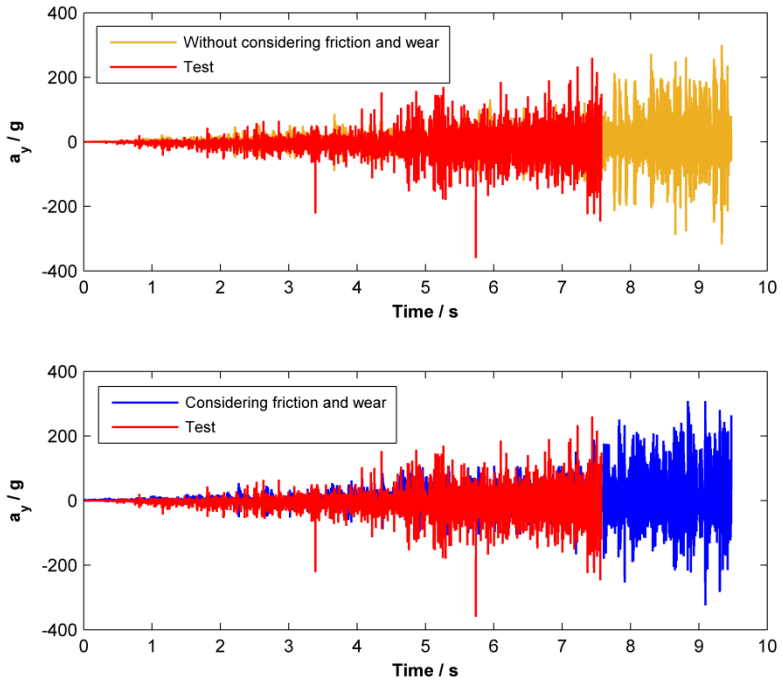

Fig. 23 Vertical acceleration

The vertical vibration acceleration of the front slipper was analysed in the time domain. To obtain the internal relationship between the vertical acceleration a_y and the sliding velocity v_x, the RMS values of the vertical acceleration in a small range under different sliding velocities were extracted as shown in Fig. 24. It was found that the RMS value of the vertical acceleration of the front slipper increased almost linearly with the sliding velocity. Compared with the computational values without considering friction and wear, the RMS values of the vertical acceleration considering friction and wear matched better with the test values, confirming the need to consider friction and wear in the hypersonic rocket sled dynamics computation. There was no significant difference between the computational results with and without considering friction and wear at low speeds, during which only a small amount of wear was generated. However, at high speeds above 800 m/s, owing to increasing wear, the RMS values of the computational vertical acceleration without considering friction and wear were smaller and different from the test values, while the computational results considering friction and wear were closer to the test values. When the sliding velocity of the rocket sled reached 1700 m/s, the RMS value of the computational vertical acceleration considering friction and wear was 78.4 g, whereas it was only 65.3 g when friction and wear were not considered. The case without considering friction and wear underestimated the RMS value by approximately 20.1%.

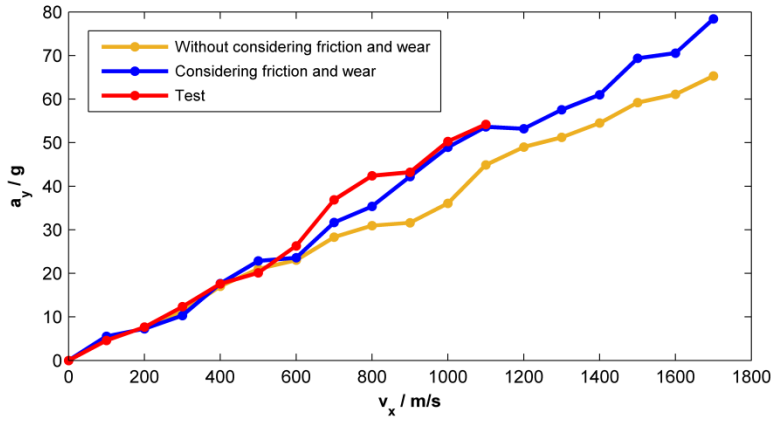

Fig. 24 RMS value of vertical acceleration vs. sliding velocity

From the above analysis, it was shown that wear had a significant influence on the vertical vibration acceleration of the front slipper. In fact, the change in the wear height in the dynamic computation of the rocket sled was reflected by the change in the slipper–track gap. Therefore, a dynamic study of the rocket sled under different slipper–track gaps was conducted. The rocket sled dynamic computational method without considering friction and wear was adopted to simulate seven working conditions, and the vertical slipper–track gap size was different under different working conditions. Figure 25 shows the RMS values of the vertical vibration acceleration of the front slipper under each working condition at Mach 5. It was found that the RMS value of the vertical vibration acceleration of the front slipper initially decreased and then increased with an increase in the slipper–track gap within the calculated range, and the acceleration reached a minimum when the slipper–track gap was 1.9 mm. The initial slipper–track gap used in the rocket sled test was 1.9 mm; therefore, the vertical acceleration of the rocket sled dynamics computation considering friction and wear was larger than that without considering friction and wear.

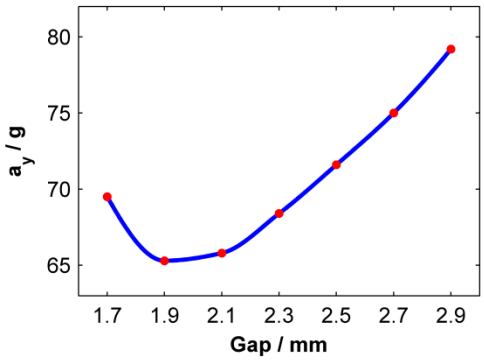

Fig. 25 RMS value of vertical acceleration vs. gap between slipper and track

As shown in Fig. 25, the best gap height existed when the vertical acceleration of the front slipper was the smallest. On the one hand, the vertical distance that the slipper can accelerate increases with an increase in the

slipper–track gap; therefore, the slipper–track collision force increases and enhances vibration. On the other hand, the influence of track irregularity on the movement of the slipper increases with a decrease in the slipper–track gap and also enhances vibration. The above analysis provides ideas for the design and optimisation of an initial slipper–track gap. There is an optimal initial slipper–track gap that can minimise the vibration magnitude of the rocket sled slipper at the maximum sliding velocity after wear to reduce vibration. However, the constraint condition of the optimal design is the minimum value of the initial slipper–track gap used to prevent the slipper from getting stuck on the track during movement.

To further analyse the dynamic response of the rocket sled in the frequency domain, time–frequency analysis was carried out on the vertical vibration acceleration test data of the third-stage sled front slipper. As shown in Fig. 26, the acceleration power spectral density (PSD) of the third-stage sled front slipper was analysed and expressed in decibels. In general, the vertical acceleration PSD of the front slipper increased with time in the full frequency band. Before 2.5 s, the vibration energy of the front slipper was mainly concentrated in the low-frequency range below 200 Hz. However, the vibration energy was distributed in the full frequency band at a high speed. This is because the average slipper–track impact force is large in the high-speed stage of a rocket sled, and the impact form is a high-frequency impact, resulting in large vibration acceleration in the full frequency band. However, the average slipper–track impact force is small in the low-speed stage of a rocket sled, and the impact form is a low-frequency impact; thus, the vibration acceleration data largely reflects the response of the third-stage sled within the first several natural frequencies below 200 Hz. In addition, as shown in Fig. 26, the energy of vibration acceleration in the full frequency band was large at t = 3.4 s and corresponded to the large slipper–track impact at t = 3.4 s as shown in Fig. 23. Therefore, it is reasonable to infer that the vibration acceleration energy in the full frequency band below 2000 Hz increases when the third-stage sled front slipper is subjected to a large impact.

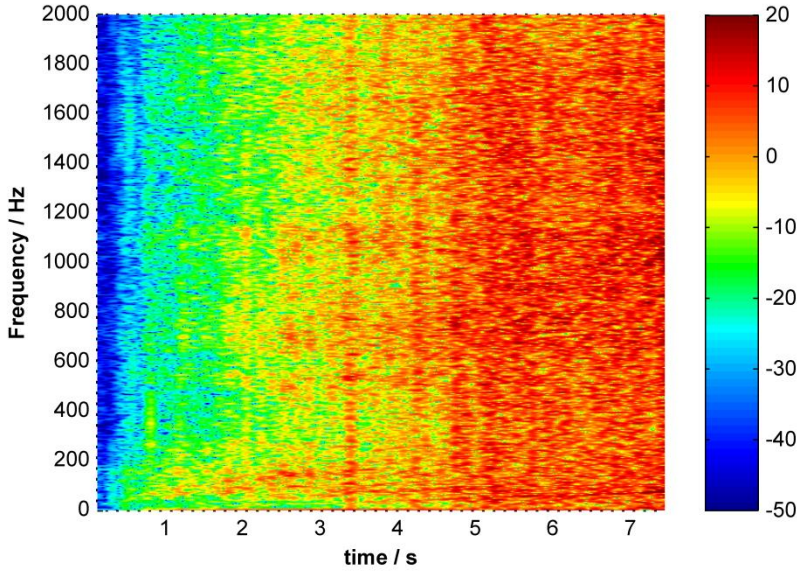

Fig. 26 Time–frequency characteristics of vertical acceleration test values

VI. Conclusion

In this study, considering the variation in the slipper–track kinetic friction coefficient and the variation in the slipper–track gap caused by wear, a multi-body dynamic computational method for time-varying and nonlinear hypersonic rocket sled system was established, and a hypersonic rocket sled test was carried out. The sliding displacement and sliding velocity of a third-stage sled predicted by the above computational method matched well with the test values. The computational RMS values of the vertical acceleration of the third-stage sled front slipper considering friction and wear matched better with the test values than the case omitting consideration. This confirms the effectiveness of the proposed computational method.

The friction and wear computational results showed that the kinetic friction coefficient decreased with an increase in the *PV* value, and the rate of decrease was high at the beginning and then decreased. The wear height of the slipper increased almost linearly with the sliding displacement of the third-stage sled. The dynamic computational results show that friction and wear had a significant effect on the pitch angle of the third-stage sled. The maximum vertical acceleration of the front slipper reached 360 g, and its RMS value increased almost linearly with the sliding velocity. The test results show that the vertical acceleration PSD of the third-stage sled front slipper increased with time in the full frequency band below 2000 Hz. The wear of the slipper in the dynamics computation was reflected by the change in the slipper–track gap. The RMS value of the vertical acceleration of the front slipper

decreased initially and then increased with an increase in the slipper–track gap, which provides useful information for the design and optimisation of the initial slipper–track gap of a rocket sled system.

In conclusion, friction and wear should be considered in the dynamic analysis of a hypersonic rocket sled system. Because of the limitations of computing resources, the rocket sled system was regarded as a rigid body in this study. Further studies will be carried out to discretize the rocket sled system and strike a balance between excessive computation and high precision. In addition, only the mechanical wear of the slipper was considered in this study; melt wear will be considered in subsequent work.

Funding Sources

This work was supported by the National Natural Science Foundation of China (grant numbers u20b2002), Project B18040, and the K. C. Wong Education Foundation.

Acknowledgments

The work was supported by HPC Platform of Xi'an Jiaotong University.

References

[1] Szmerekovsky, A. G., and Palazotto, A. N., "Structural Dynamic Considerations for a Hydrocode Analysis of Hypervelocity Test Sled Impacts," *AIAA Journal*, Vol. 44, No. 6, 2006, pp. 1350-1359. https://doi.org/10.2514/1.13803.

[2] Szmerekovsky, A. G., Palazotto, A. N., and Baker, W. P., "Scaling Numerical Models for Hypervelocity Test Sled Slipper-Rail Impacts," *International Journal of Impact Engineering*, Vol. 32, No. 6, 2006, pp. 928-946. https://doi.org/10.1016/j.ijimpeng.2004.09.011.

[3] Cinnamon, J. D., and Palazotto, A. N., "Analysis and Simulation of Hypervelocity Gouging Impacts for a High Speed Sled Test," *International Journal of Impact Engineering*, Vol. 36, No. 2, 2009, pp. 254-262. https://doi.org/10.1016/j.ijimpeng.2007.11.009.

[4] Laird, D. J., and Palazotto, A. N., "Gouge Development during Hypervelocity Sliding Impact," *International Journal of Impact Engineering*, Vol. 30, No. 2, 2004, pp. 205-223. https://doi.org/10.1016/S0734-743X(03)00059-9.

[5] Laird, D. J., and Palazotto, A. N., "Effect of Temperature on the Process of Hypervelocity Gouging," *AIAA Journal*, Vol. 41, No. 11, 2003, pp. 2251-2260.

https://doi.org/10.2514/2.6818.

[6] Minto, D. W., "CTEIP Funded Advances in Hypersonic Testing at the Holloman High Speed Test Track," AIAA Paper 2004-2740, June 2004. https://doi.org/10.2514/6.2004-2740.

[7] Minto, D. W., "Recent Increases in Hypersonic Test Capabilities at the Holloman High Speed Test Track," AIAA Paper 2000-0154, January 2000. https://doi.org/10.2514/6.2000-154.

[8] Rao, Y., "Analysis and Numerical Simulation of Several Influencing Factors on the Stability of Hypersonic Rocket Sled," Master's Dissertation, Xi'an University of Architecture and Technology, Xi'an, China, 2019, ProQuest Ebrary. (in Chinese) https://doi.org/10.27393/d.cnki.gxazu.2019.001212.

[9] Zhou, X. J., "The Dynamics Analysis Based on Simpack of Rocket Sled," Master's Dissertation, Nanjing University of Science &Technology, Nanjing, China, 2018, ProQuest Ebrary. (in Chinese) https://kns.cnki.net/KCMS/detail/detail.aspx?dbname=CMFD201901&filename=1018312616.nh

[10] Zhang, L. Q., Deng, Z. C., Guo, F. M., and Yan, J., "Study on Relation of Slide-Rail Regularity and High-Speed Movement Dynamic Response of Sled," *Journal of Ballistics*, Vol. 23, No. 2, 2011, pp. 106-110. (in Chinese) https://kns.cnki.net/kcms/detail/detail.aspx?FileName=DDXB201102025&DbName=CJFQ2011

[11] Fan, K., Yang, Z., Xue, X. M., and Xia, H. L., "Transmission Characteristics of Impact Response of Monorail Rocket Sled," *Chinese Journal of Applied Mechanics*, Vol. 37, No. 5, 2020, pp. 1887-1893+2311. (in Chinese) https://kns.cnki.net/kcms/detail/detail.aspx?FileName=YYLX202005006&DbName=CJFQ2020

[12] Minto, D. W., "The Holloman High Speed Test Track Hypersonic Upgrade Program," AIAA Paper 2002-3034, June 2002. https://doi.org/10.2514/6.2002-3034.

[13] Lim, S. C., Ashby, M. F., and Brunton, J. H., "The Effects of Sliding Conditions on the Dry Friction of Metals," *Acta Metallurgica*, Vol. 37, No. 3, 1989, pp. 767-772. https://doi.org/10.1016/0001-6160(89)90003-5.

[14] Hooser, M., "Simulation of a 10,000 Fps Ground Vehicle," AIAA Paper 2000-2290, June 2000. https://doi.org/10.2514/6.2000-2290.

[15] Hooser, M., Schwing, A., "Validation of Dynamic Simulation Techniques at the Holloman High Speed Test Track," AIAA Paper 2000-0155, January 2000. https://doi.org/10.2514/6.2000-155.

[16] Wang, J., "The Research for Coupled Dynamics of High Speed Rocket Sled-Track Systems," Ph.D. Dissertation, Nanjing University of Science &Technology, Nanjing, China, 2011, ProQuest Ebrary. (in Chinese)

https://doi.org/10.7666/d.y2060924.

[17] Zhang, J. H., Wang, J., and Zhu, Q., "Multibody System Finite Element Dynamic Analysis of Rocket Sled," *Journal of Xi'an Technological University*, Vol. 38, No. 4, 2018, pp. 377-383. (in Chinese) https://doi.org/10.16185/j.jxatu.edu.cn.2018.04.013.

[18] Gu, K. X., Gong, M. S., Wang, L., and Xiong, C., "Study on Full Time Dynamics Simulation of Two-Track Rocket Sled," *Advances in Aeronautical Science and Engineering*, Vol. 11, No. 2, 2020, pp. 245-250. (in Chinese) https://doi.org/10.16615/j.cnki.1674-8190.2020.02.014.

[19] Furlow, J. S., "Parametric Dynamic Load Prediction of a Narrow Gauge Rocket Sled," Ph.D. Dissertation, Mechanical Engineering, New Mexico State University, Las Cruces, New Mexico, 2006, ProQuest Ebrary. https://www.proquest.com/docview/86066810/FE0D96B73DC0483APQ/1?accountid=16294

[20] Lankarani, H. M., and Nikravesh, P. E., "Continuous Contact Force Models for Impact Analysis in Multibody Systems," *Nonlinear Dynamics*, Vol. 5, No. 2, 1994, pp. 193-207. https://doi.org/10.1007/BF00045676.

[21] Minh, C. N., Anthony N. P., John D. C., and Andrew G. S., "Analysis of Computational Methods for the Treatment of Material Interfaces," AIAA Paper 2005-2354, April 2005. https://doi.org/10.2514/6.2005-2354.

[22] Vereschaka, A. A., Volosova, M. A., Batako, A. D., Vereshchaka, A. S., and Mokritskii, B. Y., "Development of Wear-Resistant Coatings Compounds for High-Speed Steel Tool using a Combined Cathodic Vacuum Arc Deposition," *International Journal of Advanced Manufacturing Technology*, Vol. 84, No. 5, 2016, pp. 1471-1482. https://doi.org/10.1007/s00170-015-7808-5.

[23] Mukhopadhyay, A., Howard, I. C., and Sellars, C. M., "Development and Validation of a Finite Element Model for Hot Rolling using ABAQUS/STANDARD," *Materials Science and Technology*, Vol. 20, No. 9, 2013, pp. 1123-1133. https://doi.org/10.1179/026708304225022070.

[24] Hooputra, H., Gese, H., Dell, H., and Werner, H., "A Comprehensive Failure Model for Crashworthiness Simulation of Aluminium Extrusions," *International Journal of Crashworthiness*, Vol. 9, No. 5, 2004, pp. 449-464. https://doi.org/10.1533/ijcr.2004.0289.

[25] Roe, P. L., "Approximate Riemann Solvers, Parameter Vectors, and Difference Schemes," *Journal of Computational Physics*, Vol. 43, No. 2, 1981, pp. 357-372. https://doi.org/10.1016/0021-9991(81)90128-5.

[26] Antony J., and Scokkwan Y., "Lower-Upper Implicit Schemes with Multiple Grids for the Euler Equations," *AIAA Journal*, Vol. 25, No. 7, 1987, pp. 929-935.

https://doi.org/10.2514/3.9724.

[27] Watt, J. M., "Numerical Initial Value Problems in Ordinary Differential Equations," *The Computer Journal*, Vol. 15, No. 2, 1972, pp. 155. https://doi.org/10.1093/comjnl/15.2.155.

[28] Wei, B. H., Sun, K., Wang, Y. P., Fang, L., and Chen, C., "Finite Element Prediction for Friction Coefficient of High Speed Dry Sliding," *Journal of Xi'an Jiaotong University*, Vol. 54, No. 6, 2020, pp. 82-89. (in Chinese) https://kns.cnki.net/kcms/detail/detail.aspx?FileName=XAJT202006012&DbName=CJFQ2020

[29] Majumdar, A., and Bhushan, B., "Role of Fractal Geometry in Roughness Characterization and Contact Mechanics of Surfaces," *Journal of Tribology*, Vol. 112, No. 2, 1990, pp. 205-216. https://doi.org/10.1115/1.2920243.